Journal of Manufacturing Processes 131 (2024) 1869–1877

Contents lists available at ScienceDirect

Journal of Manufacturing Processes

journal homepage: www.elsevier.com/locate/manpro

# Fabrication and characterization of corrosion resistant amorphous-nanocrystalline alloy $Ni_{49}Co_3Mo_{22}B_{26}$ by galvanostatic deposition

M.F. Yasir, M. Sundaram *

*Department of Mechanical and Materials Engineering, University of Cincinnati, Cincinnati, OH, USA*

ARTICLE INFO

*Keywords:*
Amorphous-nanocrystalline
Corrosion
Electrodeposition
micro-hardness
Ni-alloy
Recrystallization

ABSTRACT

Amorphous materials have unique physical properties but have limited practical use due to their low ductility and thermal instability. A quaternary $Ni_{49}Co_3Mo_{22}B_{26}$ amorphous-nanocrystalline plating was prepared by electrodeposition to obtain good hardness, corrosion resistance, and thermal stability. Multiple electrolyte baths with boric acid concentration ranging from 0.3 M to 0.8 M were investigated to study the co-deposition pattern of molybdenum (Mo) and boron (B) with iron-group elements. Experimentations suggest that an array of binary, ternary, and quaternary alloys can be fabricated by adjusting boric acid concentration in an electrolyte bath. Energy Dispersive X-ray Spectroscopy (EDS) analysis shows that co-deposition of Mo requires sluggish mass transport of iron group element nickel (Ni) and cobalt (Co) and high boric acid concentration retards Mo deposition entirely. X-ray diffraction (XRD) patterns were examined to identify the formation of amorphous-nanocrystalline film deposition. An average hardness for quaternary Ni-Co-Mo-B deposit samples was measured between the range of 380 HV- 450 HV, and the hardness increases with increased B content. Electrochemical corrosion tests reveal that the addition of Mo in quaternary Ni-Co-Mo-B increases corrosion performance in saline environments but reduces corrosion performance in acidic environments over Ni-Co-B amorphous alloy. Differential scanning calorimetry (DSC) scan shows that prepared amorphous-nanocrystalline material has thermal stability up to 346 °C without undergoing phase change.

## 1. Introduction

Amorphous metals or metallic glasses also known as undercooled liquids are generally prepared by rapid quenching of metal melts [1]. Amorphous metals are characterized by their inherent lack of crystal structure, translational periodicity, and crystalline symmetry. These characteristics give them mechanical and physical properties like high hardness, brittleness, and good corrosion resistance [2]. One major drawback of amorphous metals is poor thermal stability, which is observed when the metal undergoes repeated heat treatment resulting in reversible and irreversible changes in their crystalline phases [3]. Two boundary conditions for amorphous phase formation were found: (I) free energy difference between amorphous phase and its counterpart crystalline phase should be negative or small; (II) rate of amorphous phase formation should be higher than its counterpart crystalline phase [4]. The unique characteristics of metallic glass make them attractive for applications requiring specific functional properties (corrosion resistance, soft and hard magnetic properties, catalytic properties) if their limitations are mitigated [5,6].

In the past few decades, several techniques such as mechanical alloying, conventional casting, spray deposition, electrodeposition, electroless deposition, vapor deposition, and precipitation, reduction have been developed for preparation of amorphous metals [4]. Fabrication of amorphous metals by electrodeposition techniques offers a wide selection of elements and superior control over the process parameters. Nickel-boron (Ni—B), cobalt-boron (Co—B), nickel-phosphorous (Ni—P), nickel-cobalt-boron (Ni-Co-B), iron-phosphorous (Fe—P), nickel-tungsten (Ni—W) are some of the most studied amorphous alloys. These studies reveal that non-metallic alloying elements like boron (B), phosphorous (P), carbon (C), and nitrogen (N) control crystallinity of the final product based on their composition [7,8]. Studies reported that Ni with <11 at.% B alloys exhibits crystalline structures; Ni-11 at.% B alloys contain nanocrystalline grains ranging from 1 to 3 nm; Ni-20 at.% B alloys exhibit fully amorphous structures

* Corresponding author at: University of Cincinnati, 2600 Clifton Ave, OH 45221, USA.
*E-mail address:* murali.sundaram@uc.edu (M. Sundaram).

https://doi.org/10.1016/j.jmapro.2024.09.115
Received 30 August 2023; Received in revised form 4 September 2024; Accepted 30 September 2024
Available online 12 October 2024

[9,10]. Studies show that Ni—Co based amorphous alloy can have good soft magnetic properties, which can have application in magnetic amplifiers, magnetic cores, transformers and make them a great candidate for MEMS devices and sensors [11,12]. Furthermore, amorphous/nanocrystalline materials are suitable candidates for hydrogen storage and catalytic application like petrochemical reaction, environmental remediation, and energy conservation [13,14].

Fabrication of amorphous alloys using electrochemical techniques involve co-deposition of a metalloid or non-metallic species (such as B, or P) with some metallic species (such as Ni, Co, or Fe). Commonly studied metalloid species like B and P have smaller atomic size than the metallic species such as Ni, Co, or Fe. It could be possible that the atomic size mismatch between two classes of element is the dominant factor that results in the formation of amorphous alloys. On the other hand, smaller quantities of these metalloid species are often used in crystalline alloys such as steel, nickel-based alloys produced in metallurgical methods, as a mean of solid solution strengthening in which they prefer to take interstitial position [15]. One explanation to relate these contradictions is that co-deposition of metalloid species in larger quantities forms products with highly disoriented crystals, which would explain the crystallization of amorphous alloy after hear treatment [3].

Ni—B amorphous alloys prepared by electrodeposition can have a variety of functional properties depending on the boron content. For example, low boron content (about 4 at.%) have higher corrosion resistance, which decreases as the boron content increases. At the same time, higher microhardness and wear resistance are observed with Ni—B alloy with higher boron content, suggesting an obvious tradeoff between hardness and corrosion resistance relating to boron content [9]. On the other hand, thermal stability of Ni—B alloy increases with higher Boron content, delaying the irreversible crystallization process [16]. Studies have reported that Ni—B amorphous nanoparticles of 5 nm size are air stable while retaining their physical properties as well as their magnetic properties [17]. Ternary Ni-Co-B amorphous alloys show a different trend in microhardness and corrosion resistant properties. Studies report that increased boron content in ternary Ni-Co-B amorphous alloys significantly improves mechanical properties (20 at.% B and 10 at.% Co) while improving corrosion properties due to formation of a passive nickel cobalt hydroxide film [18]. Another study on Ternary Ni-Co-P amorphous alloys reveal that the presence of cobalt in Ni-Co-P alloys improves the corrosion resistance in NaCl medium [19]. This study aims to explore the formation of Ni-Co-Mo-B alloys to investigate the multifunctionality of amorphous materials as the presence of Mo as an alloying element is known to improve corrosion performance by formation of similar passive films [20–22].

Non-conventional techniques like electrochemical additive manufacturing (ECAM) or additive electrochemical micro-manufacturing (micro-AECM) utilized the principle of localizing electrodeposition to fabricate parts of complex geometry [23–25]. These techniques often rely on boric acid ($H_3BO_3$) as a buffer to maintain the pH of the electrochemical environment and to speed up the deposition process. However, $H_3BO_3$ can also act as a source of boron which would co-deposit with metallic species under certain electrochemical conditions [26]. Such unwanted co-deposition could reduce the ductility of the manufactured parts. Therefore, the co-deposition behavior of Boron must be understood to prevent deposition of unwanted amorphous phase that could promote brittleness when fabricating structural parts. At the same time, some metallic species like Mo cannot be deposited on their own, which are co-deposited with species like Ni, Co, Fe etc. [23]. Therefore, it is also necessary to study their deposition behavior in the presence of $H_3BO_3$.

Amorphous materials are inherently brittle, which limits their usage in structural application. Conversely, engineering amorphous-nanocrystalline materials can result in materials with a combination of unique properties that can be very attractive for functional application such as environmental corrosion protection. For example, nanocrystalline metals can show enhanced mechanical properties based on Hall-Petch relationships, which states that reduction in grain size results in stronger material [27]. However, after reaching a critical threshold value, further reduction in grain size weakens the material [28]. Additive manufacturing techniques such as ECAM or micro-AECM that has the capabilities to form amorphous alloys can be used reinforce crystalline alloys (cores that provide ductility) with amorphous-nanocrystalline alloys as coating providing hardness and superior corrosion resistance. Electrodeposition based techniques has a high degree of control in manipulating the dissolution and deposition environment, has the potential to offer a diverse array of amorphous-nanocrystalline alloys.

Electrodeposition of multiple elements can be complicated and unpredictable compared to conventional metallurgical methods (i.e., melting-solidification). Each element has their own deposition rate that can vary depending on the electrochemical environment such as pH, temperature, applied potential, presence of other depositing species, electrode material, interelectrode gap and much more [29–31]. Studies reported that Ni-based surface nanocrystals in steel substrate can improve corrosion resistant properties by forming passive layer then crystalline counterparts [32]. Ni and Co surface alloying has also been proven to improve galvanic corrosion resistance at high temperature [33,34]. The presence of Mo in an alloy can increase the corrosion resistance as Mo can form passive oxide film in the outer surface which can resist corrosion against $Cl^-$ ion adsorption in saline environment [20–22]. Therefore, investigating the co-deposition behavior of B and Mo is required to fabricate amorphous-nanocrystalline alloys with high corrosion resistance and high hardness. Thus, this study aims to fabricate Ni-Co-Mo-B amorphous-nanocrystalline alloys and characterize their physical and functional properties.

**Table 1**
List of electrodeposition bath ingredients and operating conditions.

| Baseline Concentrations | |
|---|---|
| NaCl (Accelerating Agent) | 0.1 M |
| $H_2SO_4$ (Bath control Agent) | 0.01 M |
| $NiSO_4.6H_2O$ (aqueous solution) | 0.5 M |
| $CoSO_4.7H_2O$ (aqueous solution) | 0.1 M |
| $Na_2MoO_4.2H_2O$ (aqueous solution) | 0.025 M |
| $H_3BO_3$ | 0–0.8 M |
| **Operating Conditions** | |
| Temperature | 298 K |
| Deposition duration | 1200 s |
| Current density | 1–20 mA/cm$^2$ |

**Table 2**
Experiment design of electrodeposition condition and bath concentration (B.A. stands for boric acid, $H_3BO_3$).

| Bath | Current Density Baseline concentration | 1 mA/cm$^2$ | 5 mA/cm$^2$ | 10 mA/cm$^2$ | 20 mA/cm$^2$ |
|---|---|---|---|---|---|
| 1 | [Ni], [Co], [Mo], NaCl, $H_2SO_4$ | 0.3 M B.A. | 0.3 M B.A. | 0.3 M B.A. | 0.3 M B.A. |
| 2 | [Ni], [Co], [Mo], NaCl, $H_2SO_4$ | 0.4 M B.A. | 0.4 M B.A. | 0.4 M B.A. | 0.4 M B.A. |
| 3 | [Ni], [Co], [Mo], NaCl, $H_2SO_4$ | 0.5 M B.A. | 0.5 M B.A. | 0.5 M B.A. | 0.5 M B.A. |
| 4 | [Ni], [Co], [Mo], NaCl, $H_2SO_4$ | 0.8 M B.A. | 0.8 M B.A. | 0.8 M B.A. | 0.8 M B.A. |
| 5 | [Ni], [Co], [Mo], NaCl, $H_2SO_4$ | N/A | N/A | 0.0 M B.A. | N/A |
| 6 | [Ni], [Co], NaCl, $H_2SO_4$ | N/A | N/A | 0.0 M B.A. | N/A |

## 2. Materials and methods

A sulphate-chloride electrolyte bath was prepared, and the chemical

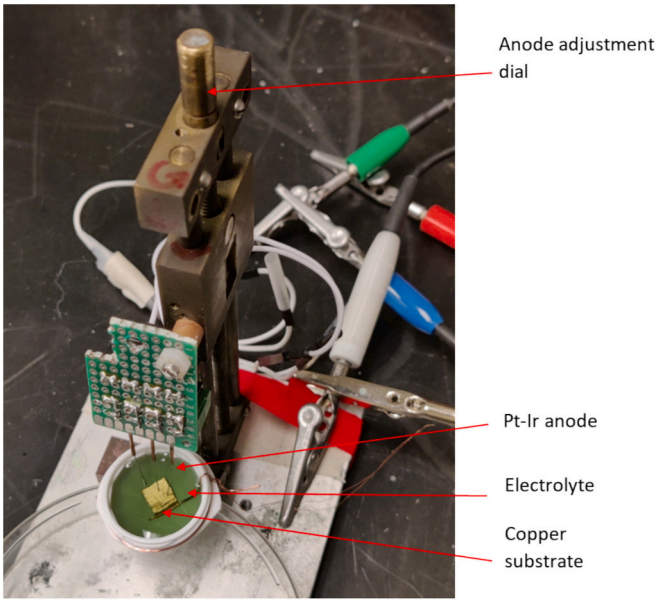


**Fig. 1.** Experimental setup and electrode configuration.

content is listed in Table 1. Chemical supporting agent such as Sodium chloride (NaCl) and sulfuric acid ($H_2SO_4$) were included in the bath to improve the deposition rate and the conductivity respectively. Sources of metallic elements consist of nickel sulphide hexahydrate ($NiSO_4.6H_2O$), cobalt sulphate heptahydrate ($CoSO_4.7H_2O$) and Sodium molybdate dihydrate ($Na_2MoO_4.2H_2O$). Boric acid ($H_3BO_3$) was added as a source of boron and as a buffer to maintain pH of bath and to improve deposition speed. Supporting bath mixture was prepared prior to addition of alloying element sources. Six electrodeposition baths were prepared as listed in Table 2 along with applied current density conditions. Bath 1–4 is targeted to investigate formation of amorphous-nanocrystalline materials and bath 5–6 were prepared for formation of Ni-Co-Mo alloy and Ni—Co alloy respectively.

An in-house build electrode setup (shown in Fig. 1) was used to perform electrochemical deposition. Copper sheets were used as substrate in each experiment, while a set of three parallel 0.25 mm platinum-iridium wire tools were used as anode. The interelectrode gap was 5 mm, which was kept constant for every trial. Electrodeposition was performed on galvanostatic mode using at constant current densities for each experiment for 20 min. Multiple deposition was performed with current densities ranging from 1 to 20 mA/cm$^2$ for each discrete solution. The weight of the substrate before and after the deposition was measured accurately with a resolution of 0.1 mg for calculation of deposition layer thickness and growth rate.

The composition analysis was done by energy dispersive x-ray

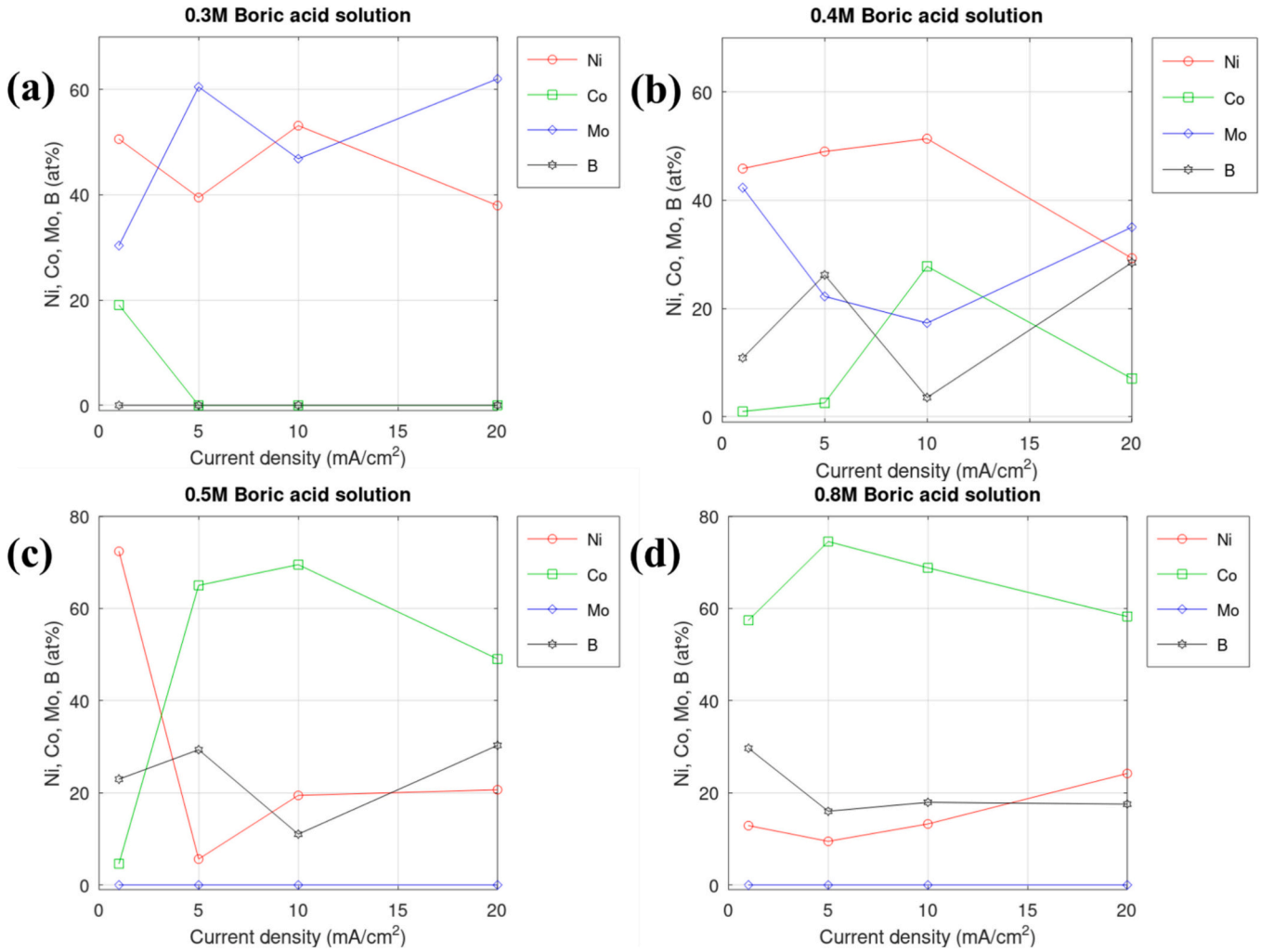


**Fig. 2.** Elemental composition (at.%) vs. current density deposited at (a) 0.3 M $H_3BO_3$ solution (b) 0.4 M $H_3BO_3$ solution (c) 0.5 M $H_3BO_3$ solution (d) 0.8 M $H_3BO_3$ solution.

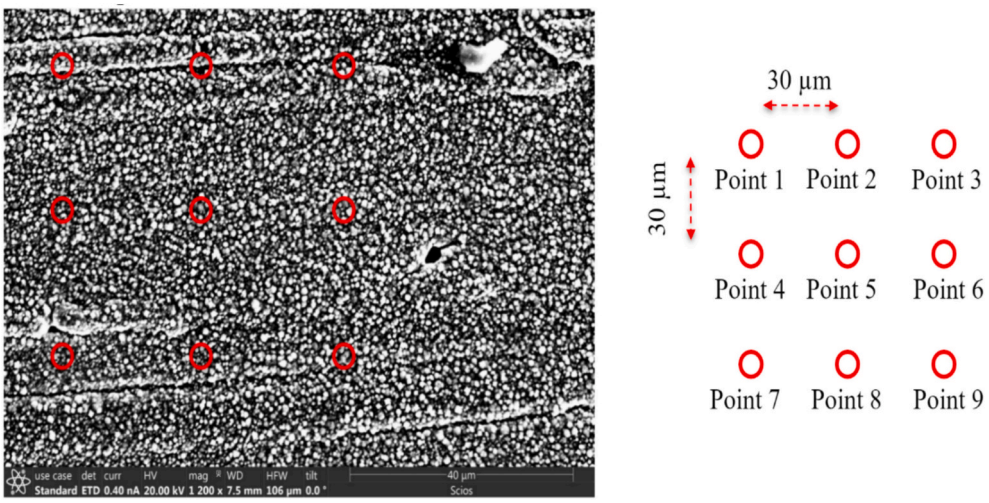


**Fig. 3.** Micrograph of deposit at 0.5 M boric acid at 10 mA/cm$^2$ and the location of EDS points.

spectroscopy (EDS) in a SCIOS dual beam scanning electron microscope (SEM) equipped with Octane Elite EDS detector. The presence of elements in the deposition was determined by analyzing EDS spectra, while quantitatively taking them into consideration. The differential scanning calorimetry (DSC) test was conducted on DSC D2500 (TA Instruments) with a temperature range of −90 °C to 550 °C. Surface morphology of the deposited alloys was examined by SEM and the crystal structure analyzed by Rigaku Smartlab XRD equipped with copper x-ray source (wavelength = 1.54056 Å). The hardness of the electrodeposited samples was measured by Wilson VH1202 micro hardness tester. Vickers indenter tool was used with a 10 g-force load to make indentation on sample surface.

## 3. Results and discussion

### 3.1. Electrodeposition results

The effects of the current density on the alloy composition are presented in Fig. 2. It was observed that an array of binary, ternary and quaternary alloys were formed, including Ni—Co, Ni-Co-B, Ni-Co-Mo and Ni-Co-Mo-B alloys. Bath 1 (0.3 M boric acid solution) is unable to deposit B. This suggests that 0.3 M $H_3BO_3$ is an insufficient quantity for B deposition. Bath 1 is however capable of depositing Ni-Co-Mo alloy with 1 mA/cm$^2$ current density. Mo is known to deposit at the presence of iron group elements, which is known as induced co-deposition [35]. It was observed that higher current densities in bath 1 is unable to deposit Mo. The experimental results suggest at exceptionally low current density, transportation of cation is slow enabling Mo to co-deposit with Ni and Co. Although source of boron was present in the bath 1, the concentration of $H_3BO_3$ is not strong enough to simultaneously co-

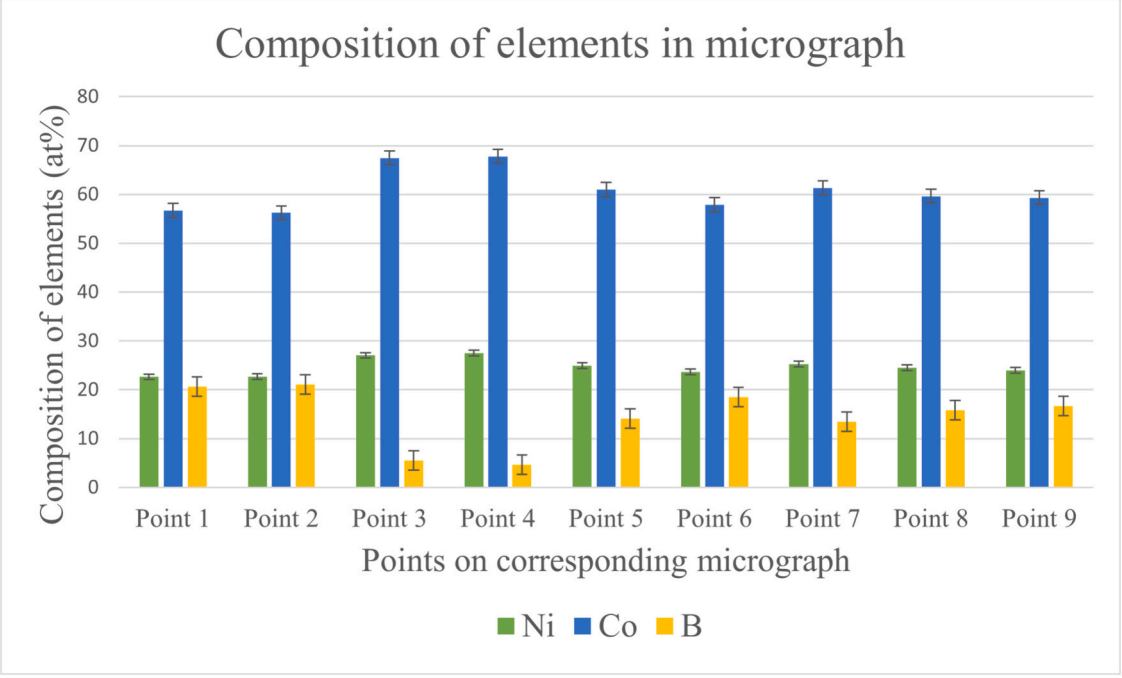


**Fig. 4.** Composition analysis at 0.5 M boric acid at 10 mA/cm$^2$.

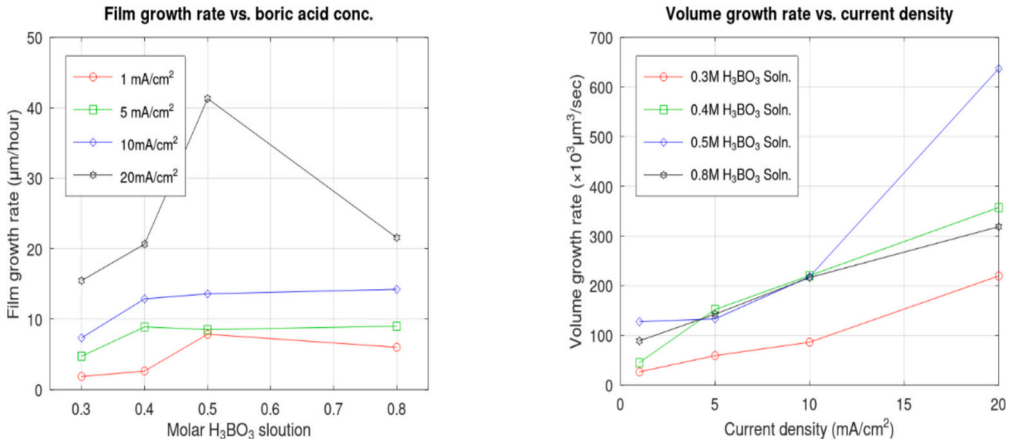


**Fig. 5.** (a) Film growth rate vs. Boric acid concentration (b) volume growth rate vs. Boric acid concentration.

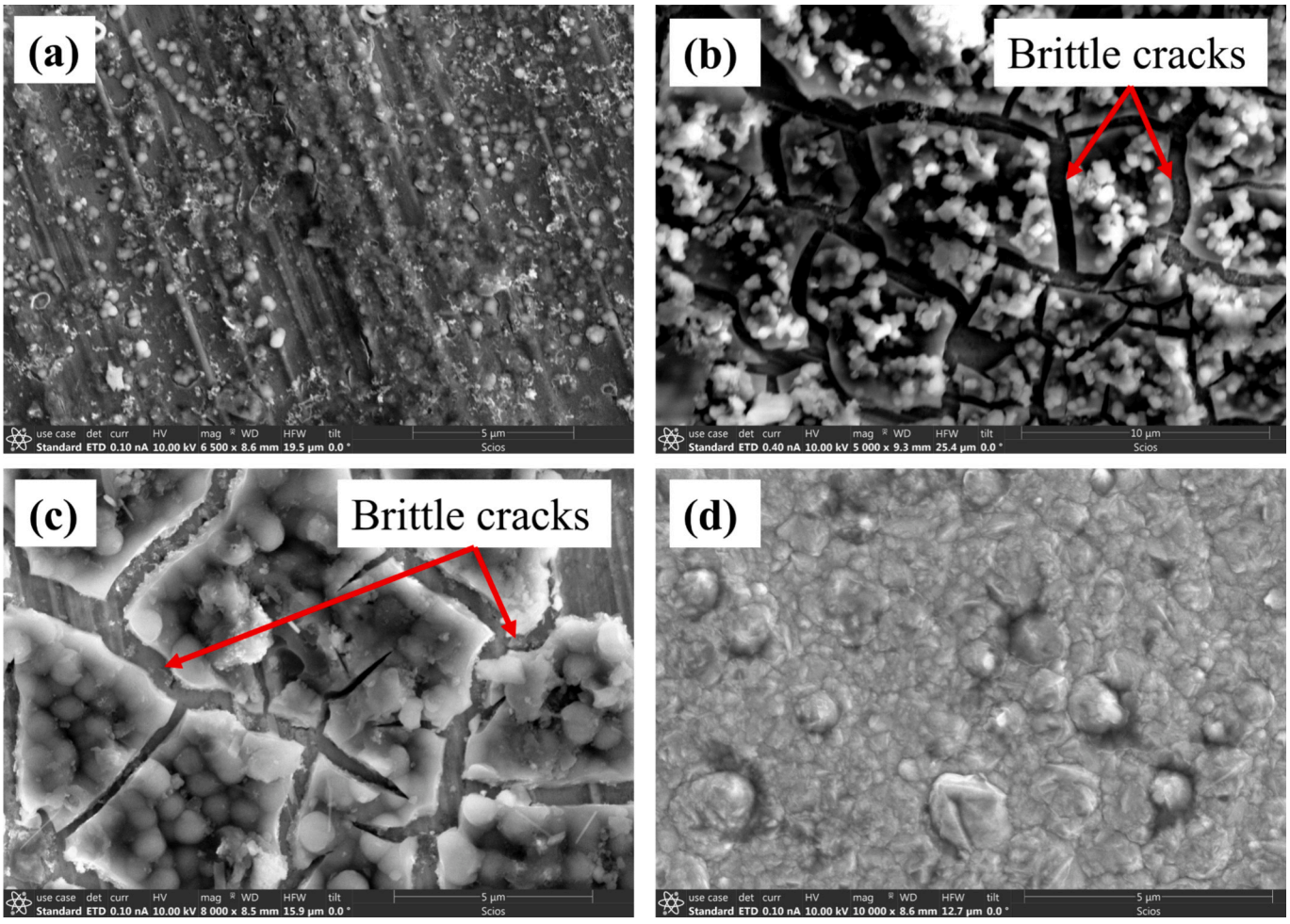


**Fig. 6.** Surface morphology of (a) 0.3 M $H_3BO_3$ solution-1 mA/cm$^2$ current density (b) 0.4 M $H_3BO_3$ solution-5 mA/cm$^2$ current density (c) 0.3 M $H_3BO_3$ solution-10 mA/cm$^2$ current density (d) 0.5 M $H_3BO_3$ solution-20 mA/cm$^2$ current density.

deposit B and Mo; suggesting it is only acting as a buffer for the electrochemical environment.

Fig. 2(b) shows that bath 2 (0.4 M boric acid solution) is capable of fabricating quaternary Ni-Co-Mo-B alloy. No robust trend was identified within the range of studied parameters. An initial increase in current density (from 1 to 10 mA/cm$^2$) increases Ni and Co composition. The iron group elements (Ni and Co) promote Mo deposition in low current density (5 mA/cm$^2$), because Mo co-deposition in the studied baths requires sluggish deposition rate, which was also observed in bath 1. At higher current density, B deposition is promoted, indicating, Ni has a higher tendency to co-deposit B compared to Co.

Bath 3 and 4 has sufficient boric acid for steady B co-deposition with Ni and Co metals. Bath 3 and 4 are unable to deposit Mo, suggesting that Mo co-deposition requires sluggish mass transport of Ni and Co. This observation agrees with the Mo co-deposition patterns in bath 1 and 2. High concentration of boric acid promotes B deposition while retarding

**Table 3**
Micro-hardness test results.

| Bath and operating condition | Alloy | Deposition layer thickness (μm) | Average hardness |
|---|---|---|---|
| 0.4 M Solution-1 mA/cm2 | $Ni_{46}Co_1Mo_{42}B_{11}$ | 6.45 | HV385.88 |
| 0.4 M Solution-5 mA/cm2 | $Ni_{49}Co_3Mo_{22}B_{26}$ | 8.11 | HV447.93 |
| 0.4 M Solution-10 mA/cm2 | $Ni_{51}Co_{28}Mo_{17}B_4$ | 11.57 | HV378.43 |

Mo deposition. Therefore, it can be perceived that Mo can alloy with Ni and Co at 0.4 M concentration of boric acid while simultaneously co-depositing with B.

### 3.2. SEM and EDS results

It is important to understand how the element of deposition is distributed within the composition to justify the accuracy of data in Fig. 2. Thus, one deposition condition was randomly selected and prepared to perform multiple composition measurements. Fig. 3 shows a micrograph of Ni-Co-B alloy (prepared using bath 3, 0.5 M Boric acid solution at 10 mA/cm$^2$ current density) with 9 points for EDS measurements, each separated by 30 um gaps. It was noticed from Fig. 4 that composition variation was insignificant. It was observed that at point 3 and 4 at.% of B had bigger error margin than initial observation. This observation can imply that using multiple small anodes does not disrupt the deposition quality compared to anodes with large surface area.

Fig. 5(a) shows the effects of boric acid concentration on the alloy film growth rate. It is apparent that the rate of film growth rate increases with increasing current density agreeing with Faraday's law. However, a significant reduction in film growth rate was observed at 0.8 M $H_3BO_3$ solution at 20 mA/cm$^2$ applied current density. This is because higher current density resulted in high hydrogen evolution, which is a phenomenal where hydrogen ions ($H^+$) in aqueous solution generate hydrogen gas ($H_2$), reducing Faradaic current efficiency. Fig. 5(b) shows that for tested samples, increasing boric acid concentration results in an increase in volume growth rate. However, increasing the $H_3BO_3$ concentration from 0.3 M to 0.4 M elevates the volume growth curve to a higher level. This is because, at 0.4 M $H_3BO_3$ solution all 4 elements were deposited simultaneously, resulting in a higher Faradaic efficiency and higher volume growth rate.

Fig. 6 shows SEM images of the surface features observed in several types of alloys, (a) Ni-Co-Mo (b) Ni-Co-Mo-B (c) Ni—Mo and (d) Ni-Co-B. Ni-Co-Mo-B and Ni—Mo alloy have brittle fractures, which are present throughout the coating. Amorphous materials such as Ni-Co-Mo-B lack periodic repeating crystal structure. As movement of dislocation is a signification source of plastic deformation, lack of long-range periodic structures in amorphous metals significantly obstructs dislocation movements are making them brittle. The film deposited at 1 mA/cm$^2$ current density seems to have incomplete coverage on substrate surface, which could be justified by its low film growth rate among the tested samples. Also, it is observed that higher current density provides a better surface finish seen at Ni-Co-B micrograph.

### 3.3. Characterization results

Average hardness values are shown in Table 3. It is to be noted that 0.4 M solution-20 mA/cm$^2$ sample was not characterized by hardness tester because of its brittleness and low adhesion to substrate. It can be observed that increase in boron content increases the Vicker microhardness value of quaternary Ni-Co-Mo-B alloy. The X-ray diffraction

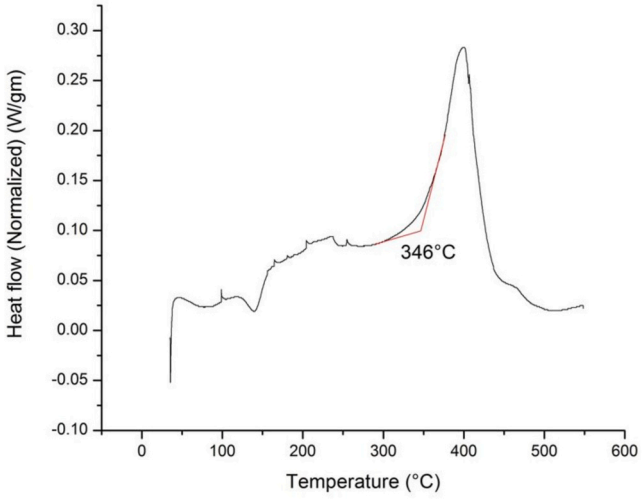


**Fig. 8.** DSC scan of Ni-Co-Mo-B alloy prepared at 10 mA/cm$^2$.

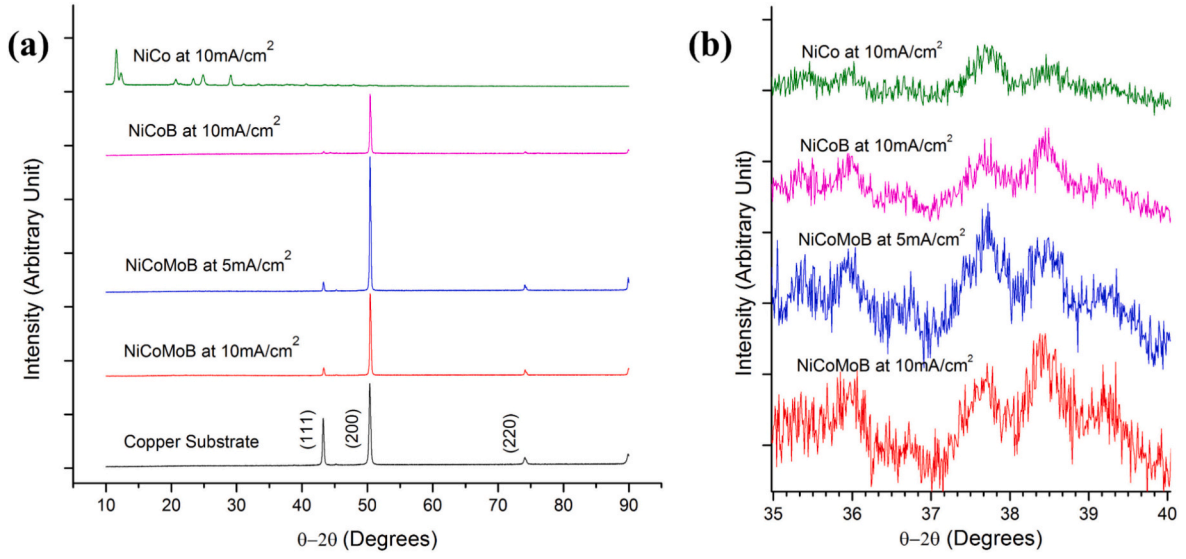


**Fig. 7.** XRD pattern of the Copper substrate and plating of Ni-Co-Mo-B at 10 mA/cm$^2$, Ni-Co-Mo-B at 5 mA/cm$^2$ Ni-Co-B at 10 mA/cm$^2$, Ni—Co at 10 mA/cm$^2$ (a) full scan and (b) zoomed peaks.

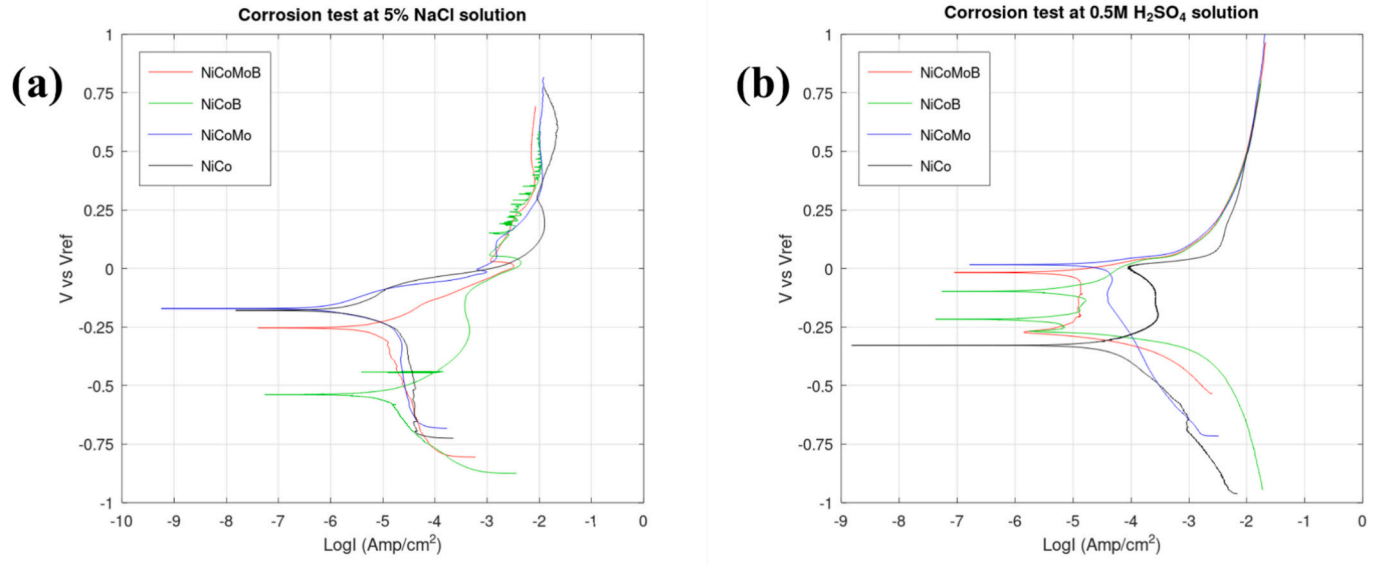


**Fig. 9.** Tafel polarization (*E*-logI) plots a) at 5 % NaCl solution b) at 0.5 M $H_2SO_4$ solution.

patterns for samples with various stoichiometry are shown in Fig. 7(a). The XRD pattern of the copper substrate was considered as reference for comparing the crystalline peaks. It can be observed that Ni-Co-Mo-B and Ni-Co-B alloys show sharp crystalline peaks located at approximately 42°, 50° and 72° which are in fact peaks diffracted by copper substrate and not the alloys themselves. These peaks are being generated by FCC copper substrate for (111), (200) and (220) crystal plane, respectively. The broader amorphous-nanocrystalline peaks can be observed after isolating the sharp crystalline peak of the substrate in Fig. 7(b). These low intensity peaks have a width of 3° (from 37° to 40°). Whereas Ni—Co alloy, which was prepared at the absence of boric acid, does not show wide amorphous peaks. It can be concluded that the absence of sharp and defined peaks throughout the scan of deposits Ni-Co-Mo-B alloys and Ni-Co-B alloy can be defined as amorphous-nanocrystalline materials, while Ni—Co alloy is crystalline.

Fig. 8 shows the DSC scan which was conducted to measure heat flow difference between sample and reference, keeping rate of change of temperature constant such that,

$$\frac{\Delta dH}{dt} = \left(\frac{dH}{dt}\right)\text{sample} - \left(\frac{dH}{dt}\right)\text{reference} \quad (1)$$

The heating rate was kept at 10 °C/min while scanning from 35 °C to 550 °C. The sample pan contained copper foil substrate, and a deposition of Ni-Co-Mo-B alloy prepared at 10 mA/cm$^2$ and the reference pan contained only copper foil substrate without any deposit. An exothermic process will release heat which is represented in the upper half of the plot. In any crystallization process material will move towards a lower energy state which releases heat energy. The crystallization process observed during the scan starts at an onset temperature of 346 °C. This suggests that the amorphous phase of Ni-Co-Mo-B alloy went through an irreversible recrystallization process.

### 3.4. Potentiodynamic polarization results

Fig. 9 shows the potentiodynamic polarization plots of amorphous-nanocrystalline alloys and crystalline alloys in 5 % NaCl solution and 0.5 M $H_2SO_4$ solution. The potentiodynamic polarization scan was conducted using an Ag/AgCl reference electrode and Platinum counter electrode in both solutions. The scan was performed from −1 to +1.5 V vs $V_{ref}$ with a sweep speed of 0.25 mV/s. Electrochemical corrosion rate measurements and mass loss rate measurements are performed in terms of corrosion current density based on Faraday's law. Standardized test

**Table 4**
Corrosion properties of amorphous-nanocrystalline and counterpart crystalline alloys.

| Alloy | Solution | Corrosion Potential, $E_{corr}$ (mV) | Corrosion current density $I_{corr}$ (mA) |
|---|---|---|---|
| Ni-Co-Mo-B | 5 % NaCl | −253.7 | 1.84 |
| Ni-Co-B | 5 % NaCl | −176.2 | 3.58 |
| Ni-Co-Mo | 5 % NaCl | −171.4 | 1.03 |
| Ni-Co | 5 % NaCl | −179.2 | 1.22 |
| Ni-Co-Mo-B | 0.5 M $H_2SO_4$ | −18.35 | 7.39 |
| Ni-Co-B | 0.5 M $H_2SO_4$ | −220.2 | 2.83 |
| Ni-Co-Mo | 0.5 M $H_2SO_4$ | 14.91 | 19.77 |
| Ni-Co | 0.5 M $H_2SO_4$ | −339.4 | 12.78 |

methods such as ASTM G-102 provides corrosion rate measurement equations and constants for repeatable calculation as shown in Eqs. (2)–(4).

$$\textit{Corrosion rate}\ (mm/year) = 3.27 \times 10^{-3} \times \frac{I_{corr}}{\rho} \times EW \quad (2)$$

$$\textit{Mass loss rate}\ \left(gm/m^2 day\right) = 0.8953 \times I_{corr} \times EW \quad (3)$$

where, $I_{corr}$ is the corrosion current density, ρ is the density of the alloy and EW is the equivalent weight defined as.

$$\textit{Equivalent weight}\ (gm) = \sum \frac{W_i}{n_i F_i} \quad (4)$$

where $W_i$, $n_i$, $F_i$ are the atomic weight, valence, and mass fraction of the alloy, respectively. The corrosion current density and corrosion potential are extracted from polarization plots by identifying convergence point of anodic and cathodic slope. However, measuring the equivalent weight for elements having multiple valencies can be problematic and unreliable, hence measuring the corrosion rate is also unreliable. On the other hand, fair comparison can be conducted for materials having similar elements fabricated from similar electrolyte baths as their equivalent weight would be similar. Therefore, materials having lower

corrosion current density will lower corrosion rate and higher corrosion performance based on Eqs. (2)–(3).

It can be observed from Table 4 that for 5 % NaCl solution, quaternary Ni-Co-Mo-B alloy had lower corrosion current density than ternary Ni-Co-B alloy and ternary Ni-Co-Mo have lower corrosion current than binary Ni—Co alloy. The results clearly suggest that addition of Mo in amorphous-nanocrystalline alloys improve corrosion performance. This is because Mo is known to form passivation films in $Cl^-$ environment, which retards further corrosion [20–22]. On the other hand, in acidic environment quaternary Ni-Co-Mo-B alloy had Higher corrosion current density than ternary Ni-Co-B. This is because Mo does not form passivation film in $SO_4^{-2}$ ion. In this situation, Ni and Co tends to form their hydroxide films with retards corrosion process [18]. The results suggests that amorphous-nanocrystalline alloys have better corrosion performance in saline environment and poor corrosion performance in acidic environment than their crystalline counterpart.

## 4. Conclusion

The study on electrodeposition of Ni-Co-Mo-B amorphous-nanocrystalline alloy was conducted with boric acid in galvanostatic mode. The results showed that electroplating parameters such as current density and boric acid concentration have a considerable influence on the formation of different alloys with compositional variations. The co-deposition of Mo and B takes place in 0.4 M $H_3BO_3$ solution along with iron group element Ni and Co. Lowering the $H_3BO_3$ concentration does not result in co-deposition of B and raising the concentration of $H_3BO_3$ does not result in the co-deposition of Mo. The optimum composition of the quaternary alloy is $Ni_{49}Co_3Mo_{22}B_{26}$ alloy. The hardness of the quaternary alloy depends on boron content, increase of B leads to an increase of Vicker's microhardness ranging from 380 to 450 HV. The absence of sharp and defined peaks in the Ni-Co-Mo-B and Ni-Co-B alloy deposits suggests that they are amorphous-nanocrystalline materials while Ni—Co alloy is crystalline. The Presence of Mo was found to improve the corrosion resistance of the Ni-based alloy in a saline environment but reduces corrosion resistance in an acidic environment compared to its crystalline counterpart due to the formation of a passive oxide film on the outer surface. The prepared quaternary materials have thermal stability up to 346 °C.

## CRediT authorship contribution statement

**M.F. Yasir:** Data curation, Formal analysis, Investigation, Methodology, Software, Validation, Visualization, Writing – original draft. **M. Sundaram:** Conceptualization, Data curation, Formal analysis, Funding acquisition, Investigation, Methodology, Project administration, Resources, Supervision, Writing – review & editing.

## Declaration of competing interest

The authors declare the following financial interests/personal relationships which may be considered as potential competing interests: Murali Sundaram reports financial support was provided by National Science Foundation. Dr. Murali Sundaram is an Associate Editor of the Journal of Manufacturing processes.

## Acknowledgements

This work was supported by the National Science Foundation under grant CMMI-1955842. Any opinions, findings, and conclusions, or recommendations expressed in this material are those of the author(s) and do not necessarily reflect the views of the National Science Foundation.

## References

[1] Klement W, Willens RH, Duwez PE. Non-crystalline Structure in Solidified Gold–Silicon Alloys. Nature 1960;187:869–70.
[2] Souza CAC, May JE, Machado AT, Tachard ALR, Bidoia ED. Preparation of Fe–Cr–P–Co amorphous alloys by electrodeposition. Surf Coat Technol 2005;190 (1):75–82. 2005/01/03/, https://doi.org/10.1016/j.surfcoat.2004.04.070.
[3] Mirak M, Akbari A. Microstructural characterization of electrodeposited and heat-treated Ni-B coatings. Surf Coat Technol 2018;349:442–51. 2018/09/15/, https://doi.org/10.1016/j.surfcoat.2018.06.022.
[4] Warlimont H. Amorphous metals driving materials and process innovations. Mater Sci Eng A 2001;304-306:61–7. 2001/05/31/, https://doi.org/10.1016/S0921-5093(00)01450-7.
[5] Yoshizawa Y, Oguma S, Yamauchi K. New Fe-based soft magnetic alloys composed of ultrafine grain structure. J Appl Phys 1988;64(10):6044–6. https://doi.org/10.1063/1.342149.
[6] Herzer G. Grain structure and magnetism of nanocrystalline ferromagnets. IEEE Transactions on Magnetics 1989;25(5):3327–9. https://doi.org/10.1109/20.42292.
[7] Djokić SS. Electrodeposition of amorphous alloys based on the iron group of metals. J Electrochem Soc 1999;146(5):1824. 1999/05/01, https://doi.org/10.1149/1.1391850.
[8] Ali M, Ahmad F. A review of processing techniques for Fe-Ni soft magnetic materials. Mater Manuf Process 2019;34(14):1580–604. 2019/10/26, https://doi.org/10.1080/10426914.2019.1662038.
[9] Bekish YN, Poznyak SK, Tsybulskaya LS, Gaevskaya TV. Electrodeposited Ni–B alloy coatings: structure, corrosion resistance and mechanical properties. Electrochim Acta 2010;55(7):2223–31. 2010/02/28/, https://doi.org/10.1016/j.electacta.2009.11.069.
[10] Lee KH, Chang D, Kwon SC. Properties of electrodeposited nanocrystalline Ni–B alloy films. Electrochim Acta 2005;50(23):4538–43. 2005/08/25/, https://doi.org/10.1016/j.electacta.2004.03.067.
[11] Gutfleisch O, Willard MA, Brück E, Chen CH, Sankar SG, Liu JP. Magnetic materials and devices for the 21st century: stronger, lighter, and more energy efficient. Adv Mater 2011;23(7):821–42. https://doi.org/10.1002/adma.201002180.
[12] Silveyra JM, Ferrara E, Huber DL, Monson TC. Soft magnetic materials for a sustainable and electrified world. Science 2018;362(6413). https://doi.org/10.1126/science.aao0195. p. eaao0195.
[13] Li FC, et al. Amorphous–nanocrystalline alloys: fabrication, properties, and applications. Mater Today Adv 2019;4:100027. 2019/12/01/, https://doi.org/10.1016/j.mtadv.2019.100027.
[14] Zhang Y, Shao Z, Zhang Y. Preparation of Mo-doping LiFePO4/C by carbon reduction method. Mater Manuf Process 2021;36(4):419–25. 2021/03/12, https://doi.org/10.1080/10426914.2020.1843669.
[15] Cheng X, et al. Interstitial-boron solution strengthened WB3+x. Appl Phys Lett 2013;103(17). https://doi.org/10.1063/1.4826485.
[16] Li H, Li H, Dai W, Qiao M. Preparation of the Ni-B amorphous alloys with variable boron content and its correlation to the hydrogenation activity. Appl Catal Gen 2003;238(1):119–30. 2003/01/08/, https://doi.org/10.1016/S0926-860X(02)00342-3.
[17] Wen M, Li L-J, Liu Q, Qi H-Q, Zhang T. The preparation of well-dispersed Ni–B amorphous alloy nanoparticles at room temperature. J Alloys Compd 2008;455(1):510–5. 2008/05/08/, https://doi.org/10.1016/j.jallcom.2007.07.074.
[18] Bekish YN, Poznyak SK, Tsybulskaya LS, Gaevskaya TV, Kukareko VA, Mazanik AV. Electrodeposited Ni–Co–B alloy coatings: preparation and properties. J Electrochem Soc 2014;161(12):D620. 2014/08/08, https://doi.org/10.1149/2.1151410jes.
[19] Parente MMV, Mattos OR, Díaz SL, Neto PL, Miranda FJF. Electrochemical characterization of Ni–P and Ni–Co–P amorphous alloy deposits obtained by electrodeposition. J Appl Electrochem 2001;31(6):677–83. 2001/06/01, https://doi.org/10.1023/A:1017573720008.
[20] Shi Y, Yang B, Liaw PK. Corrosion-resistant high-entropy alloys: a review. Metals 2017;7(2):43 [Online]. Available: https://www.mdpi.com/2075-4701/7/2/43.
[21] Chen YY, Duval T, Hung UD, Yeh JW, Shih HC. Microstructure and electrochemical properties of high entropy alloys—a comparison with type-304 stainless steel. Corros Sci 2005;47(9):2257–79. 2005/09/01/, https://doi.org/10.1016/j.corsci.2004.11.008.
[22] Chou YL, Yeh JW, Shih HC. Effect of inhibitors on the critical pitting temperature of the high-entropy alloy Co1.5CrFeNi1.5Ti0.5Mo0.1. J Electrochem Soc 2011;158 (8):C246. 2011/06/22, https://doi.org/10.1149/1.3600348.
[23] Sundaram M, Brant A, Rajurkar K. Electrochemical additive manufacturing of NiCoFeCuMo high entropy alloys using a combined dissolution-deposition system. CIRP Annals 2022;71(1):153–6. 2022/01/01/, https://doi.org/10.1016/j.cirp.2022.03.009.
[24] Brant A, Sundaram M. Electrochemical additive manufacturing of graded NiCoFeCu structures for electromagnetic applications. Manufacturing Letters 2022;31:52–5. 2022/01/01/, https://doi.org/10.1016/j.mfglet.2021.06.003.
[25] Manukyan N, Kamaraj A, Sundaram M. Localized electrochemical deposition using ultra-high frequency pulsed power. Procedia Manufacturing 2019;34:197–204. 2019/01/01/, https://doi.org/10.1016/j.promfg.2019.06.139.
[26] Sakita A, Noce R, Magnani M, Fugivara C, Benedetti A. Electrodeposition of Ni-B and Ni-Co-B alloys by using boric acid as boron source. ECS Electrochemistry Letters 2014;3:D10–2. 03/25, https://doi.org/10.1149/2.011405eel.
[27] Cordero ZC, Knight BE, Schuh CA. Six decades of the Hall–Petch effect – a survey of grain-size strengthening studies on pure metals. Int Mater Rev 2016;61(8):495–512. 2016/11/16, https://doi.org/10.1080/09506608.2016.1191808.

[28] C. S. Pande and K. P. Cooper, "Nanomechanics of Hall–Petch relationship in nanocrystalline materials," Progress in Materials Science, vol. 54, no. 6, pp. 689–706, 2009/08/01/ 2009, doi:https://doi.org/10.1016/j.pmatsci.2009.03.008.

[29] Li X, Ming P, Ao S, Wang W. Review of additive electrochemical micro-manufacturing technology. Int J Mach Tool Manuf 2022;173:103848. 2022/02/01/, https://doi.org/10.1016/j.ijmachtools.2021.103848.

[30] Wang F, Bian H, Xiao Y. Fabrication of micro-sized copper columns using localized electrochemical deposition with a 20 μm diameter micro anode. ECS Journal of Solid State Science and Technology 2019;8(4):P223. 2019/04/18, https://doi.org/10.1149/2.0111903jss.

[31] J D, P H. Investigation of electrochemical machining on SS304 using NaCl and NaNo3 as electrolyte. Mater Manuf Process 2022;37(15):1790–803. 2022/11/18, https://doi.org/10.1080/10426914.2022.2065002.

[32] Chen X, Dai X, Qian H, Yang B, Zhao J. Effects of surface nanocrystallization on the oxide film formed on 316LN stainless steel in a high-temperature aqueous environment. Materials and Corrosion 2022;73(1):125–33. https://doi.org/10.1002/maco.202112652.

[33] Gao Q, et al. Isothermal oxidation behavior of W-free Co–Ni–Al-based superalloy at high temperature. Materials and Corrosion 2022;73(4):513–25. https://doi.org/10.1002/maco.202112789.

[34] Gao L, Han F, Chen S, Ye X-X, Leng B. High-temperature corrosion behavior of Inconel 617 with Ni-claddings in molten FLiNaK salt. Materials and Corrosion 2022;73(4):486–96. https://doi.org/10.1002/maco.202112757.

[35] Eliaz N, Gileadi E. Induced Codeposition of alloys of tungsten, molybdenum and rhenium with transition metals. In: Vayenas CG, White RE, Gamboa-Aldeco ME, editors. Modern aspects of electrochemistry. New York, NY: Springer New York; 2008. p. 191–301.